arXiv:1904.05983v1 [astro-ph.SR] 11 Apr 2019

Proper Motions and Shock Wave Dynamics in the HH 7-11 Stellar Jet

P. Hartigan and R. Holcomb[1],

and

A. Frank[2]

Received _____; accepted _____

[1]Physics and Astronomy Dept., Rice University, Houston, TX

[2]Physics and Astronomy Dept., University of Rochester, Rochester NY

ABSTRACT

We have used the Hubble Space Telescope to acquire new broad-band and narrow-band images of the optical line emission and red continuum associated with the HH 7-11 stellar jet in the NGC 1333 star formation region. Combining the new narrow-band images of Hα, [O I] λ6300 and [S II] λ6716 allows us to measure electron densities and excitations at each point in the outflow with the spatial resolution of HST, while the I-band image traces out the boundary of the cavity evacuated by the outflow. Comparing these images with those taken $\sim$ 20 years ago yields high precision proper motions for all the HH objects in the outflow. HH 11 is a bullet-like clump, and emerges from the exciting source SVS 13A towards the Earth at 24 degrees to line of sight. In contrast, HH 8 and HH 10 consist of two rings of shocked gas that show no bulk proper motions even though the emitting gas is blueshifted. The HH 8 rings are expanding with time. These shocks mark places where ambient material located along the path of the jet redirects the outflow. HH 7 consists of multiple shells, and emits strongly in H_2 in what appears to be a terminal bow shock for the outflow, implying that the jet has yet to fully break out of its nascent cloud core. The jet largely fragments into clumps by the time it reaches HH 7. As in the case of HH 110, deflection from ambient material plays a key role in producing observable shock waves in the HH 7-11 outflow.

Subject headings: — stars: formation

1. Introduction

Collimated jets arise from accretion disks in a variety of astrophysical systems, including compact objects and galactic nuclei (e.g. Romero et al. 2017), and young stars (see Frank et al. 2014, for a review). Material within an accretion disk loses angular momentum as it drifts inward onto the central source, and jets play a primary role in removing this angular momentum from the system in most modern numerical models (Zanni & Ferreira 2013; Nolan et al. 2017, e.g.). Jets from young stars also affect star formation within a dark cloud by reshaping the surrounding medium as the outflows entrain ambient material and evacuate large cavities within dark clouds. The dense shells of shocked gas that form at the interfaces between the jet and the dark cloud deposit energy and momentum into the cloud, and provide a source of turbulence that opposes the gravitational forces responsible for creating new stars (Frank 2007, e.g.). As jets drive shells and cavities, they contribute to the complex geometry of clumps and filaments observed within dark clouds (e.g. Dhabal et al. 2018).

In many ways it is easiest to study collimated outflows in young stars because shock waves in young stellar jets typically cool radiatively, so the resulting emission lines make it possible to identify the locations and morphologies of the shocks, and we can obtain maps of densities and temperatures throughout the flow. In addition, many young stellar jets exhibit measurable proper motions and spectral variations over a timespan of several years, so one can observe how the flows evolve in real time (Hartigan et al. 2011). The ability to identify shocks observationally and follow them over time creates a critical connection with studies of dynamical instabilities in numerical and laboratory work (Frank et al. 2014; Hartigan et al. 2016).

In the past two decades, the spatial resolution afforded by HST has transformed our understanding of jets from young stars. Because shocks in stellar jets typically move into

neutral gas, Balmer line emission occurs both in a thin shell excited by collisions at the shock front as well as within an extended recombination zone if the shock is strong enough to ionize hydrogen. HST images of jets are able to resolve the difference in position between the Balmer shell and the regions where forbidden lines such as [S II] and [O I] emit (Heathcote et al. 1996). Such images also provide a means to identify the direction that the gas flows through the shock. HST observations of time-variable hot-spots have been identified with shock intersections (Hartigan et al. 2011, 2016), and there are now observations of temporal variability in several emission line ratios (Raga et al. 2016). Resolving the size of cooling zones has led to new theoretical work, allowing Alfvénic Mach numbers to be measured in jets (Hartigan & Wright 2015). In addition, spatially-resolved determinations of temperature and density maps as well as precise measures of jet collimation within 50 AU of the star (Hartigan & Morse 2007; de Colle et al. 2010) continue to provide major constraints on disk wind models. Many outstanding questions remain, including the nature of the magnetic geometry and collimation close to the source, the roles accretion disks and photoevaporative flows play in altering the formation of planetesimals, and how the narrow jet interacts with its surroundings and drives a molecular flow. This last topic is the main focus of this paper.

Located at a distance of $\sim$ 300 pc (de Zeeuw et al. 1999; Belikov et al. 2002, section 4), the Herbig-Haro objects HH 7-11 were among the first of their class to be catalogued (Herbig 1974), and represent one of the first known examples of a bipolar molecular outflow (Snell & Edwards 1981). A bright, variable infrared source SVS 13A (Strom et al. 1976, sometimes denoted SSV 13) drives a blueshifted jet in the direction of the HH 7-11 outflow (Hodapp & Chini 2014). SVS 13A is in fact a close binary separated by only 0.3 arcseconds (VLA 4A and VLA 4B; Anglada et al. 2000), and there is evidence from high-resolution SiO and SO maps that both stars drive outflows aligned nearly parallel to one another (Lefévre et al. 2017).

Fig. 1 shows the overall morphology of the HH 7-11 outflow. Proceeding down the HH flow away from the source, HH 11 appears as a compact knot, HH 8 and 10 are more extended, and HH 7 is a resolved bow shock. HH 9 is displaced significantly to the north of the other HH objects. HH 11 has a higher blueshifted radial velocity (~ -200 km s^{-1}) compared with HH 7, 8, 9, and 10 (~ -50 km s^{-1}), but all the HH objects have modest line widths ($\lesssim 100$ km s^{-1}; Solf & Böhm 1987). HH 7-11 are unusual compared with other HH knots in that they have very low-excitation spectra that show strong [O I] and [S II], weak [N II], and no [O III] (Böhm et al. 1983). These spectra indicate low shock velocities of ~ 30 km s^{-1} where the emitting gas is mostly neutral (Hartigan et al. 1987; Dopita & Sutherland 2017).

Because HH 7, HH 8, and HH 10 also radiate strongly in near-IR H_2 quadrupole lines (Garden et al. 1990; Khanzadyan et al. 2003), these sources are among the best examples to study shocked cooling zones that possess both molecular and optical line emission. High-resolution ground-based spectra of multiple H_2 lines in HH 7 imply a thermal population generally consistent with a simple C-shocks and inconsistent with fluorescence, though there is a weak high-temperature component at ~ 5000 K that could arise from molecular formation on dust (Pike et al. 2016; Geballe et al. 2017). Molecular lines in HH 7 are also strong in the mid-IR, and enable studies of ortho/para H_2 and HD/H_2 ratios (Yuan & Neufeld 2011; Yuan et al. 2012).

When combined with emission-line ratio maps and spectral line profiles, proper motions of spatially-resolved HH shocks create a comprehensive data set that characterizes the dynamics of the shocked gas. However, it has been difficult to measure proper motions in the HH 7-11 outflow because the velocities are low and because a typical field of view for many instruments includes few stars suitable for alignment. Low-spatial resolution observations from Spitzer at 4.5μm suggest proper motions $\lesssim 10$ km s^{-1} (Raga et al. 2012),

consistent with revised measurements in H_2 that take into account the photocenter shift of SVS 13A between epochs (Khanzadyan et al. 2003). Existing ground-based optical proper motions are also low, ~ 50 km s^{-1} directed away from SVS 13A for HH 11, with smaller values of ~ 30 km s^{-1} or less indicated for the other HH objects (Herbig & Jones 1983; Noreiega-Crespo & Garnavich 2001). Low proper motions such as these can only be measured accurately with high spatial-resolution images such as those from HST or with ground-based AO systems. Recent near-IR AO images of the immediate vicinity of SVS 13A uncovered a remarkable series of nested cavities along the blueshifted jet, with proper motions measured to be 28 km s^{-1} (taking the distance to be 300 pc; Hodapp & Chini 2014). These cavities correspond with the bullets of high velocity molecular gas seen in SiO (Lefévre et al. 2017).

In this paper we present new narrowband HST images of the HH 7-11 outflow in the lines of [O I] λ6300, Hα, and [S II] λ6716, together with a narrowband continuum image at R and a broadband continuum image at I. These are the first optical narrowband HST images to include all of HH 7, and the first study to make use of the WFC3 Quad filter on HST to isolate the [S II] λ6716 line for stellar jet work. The new images allow us to measure high-precision proper motions across the region, and by combining [S II] λ6716 with [O I] λ6300 (and [S II] λ6716 with an archival [S II] $\lambda\lambda$6716+6731 image) we compute maps of the electron density at the spatial resolution of HST ($0.07''$; ~ 20 AU at 300 pc) across the entire outflow. We also observe where the shock excitations are highest from the ratio map of Hα / ([O I] λ6300 + [S II] λ6716).

In what follows, Sec. 2 describes the data reduction and analysis procedures, and Sec. 3 presents the new HST images and ratio maps. New images of extended young stellar objects in the field, including a close binary are in Sec. 4, and Sec. 5 derives new proper motion measurements for the region. We collect these data together in Sec. 6, and summarize the

paper in Sec. 7.

2. Data Reduction

We acquired new images of the HH 7-11 flow in [O I] λ6300 (F631N; 5779 seconds), Hα (F656N; 5778 seconds), narrowband R-continuum (F645N; 2787 seconds), broadband I (F850LP; 2725 seconds), and [S II] λ6716 (FQ672N; 5778 seconds) with the WFC3 camera on the Hubble Space Telescope between Dec 11, 2017 and Jan 12, 2018. The field of view includes the driving source SVS 13A, the entire HH 7-11 outflow, and several stars to the north and west of SVS 13A. FQ672N is a 'quad' filter with a reduced field of view, but it is possible to fit the entire HH 7-11 outflow in the field with the proper orientation restrictions (Fig. 1). The filters for [O I] λ6300, Hα, and [S II] λ6716 are narrow enough to isolate these lines individually (Sec. 3), but broad enough to include the most blueshifted line emission in the flow. The narrowband continuum filter excludes all emission lines (FWHM 85 Å), and was used to verify that no continuum was present in the HH objects when calculating ratio images between emission lines in the R-band. The I-band filter (a Sloan DSS z′), includes a mixture of continuum and emission lines, and is suitable for showing morphologies of both HH objects and reflected-light cavities.

Image reductions followed the standard WFC3 pipeline procedures, and produce output images in units of electrons/sec. To calculate image ratios we need to correct for the different throughputs in each filter at the wavelength of the emission line, which are 0.232, 0.222, and 0.242, respectively, for [O I] in F631N, Hα in F656N, and [S II] λ6716 in FQ672N (Dressel 2019). The images were aligned to one-another using the geomap and geotran packages in IRAF, allowing for rotations and translations between the HST images, and also for a constant scale factor in the H_2. Typically only ~ 7 stars are in common between the narrowband HST images owing to high extinction in the region. Only three

stars are present in the quad filter. The rms registration errors between the narrowband HST images is 0.2 pixels ($\sim$ 0.008 arcseconds).

We supplemented our data with a ground-based H_2 image of HH 7-11 taken Jan 1, 2007 in 0.7 arcsecond seeing as part of the the UKIDSS survey (Lucas et al. 2008). We used the F850LP filter to align with the H_2 image because these images share the most stars, though we had to remove some embedded extended sources from the fit because extinction from circumstellar disks and envelopes caused the optical and near-infrared photocenters to differ. Overall, registration of the H_2 image is good to about 0.2 arcseconds. For reference, motions of 20 $\mathrm{km\,s^{-1}}$ over the 11-year time interval between the UKIDSS and HST images amounts to 0.15 arcseconds. No alignment stars are present in the immediate vicinity of HH 7.

3. Difference Images and Emission Line Ratio Maps

The top-left panels of Figures 2, 3, and 4 present color composites of the new HST images of HH 7, HH 8 and HH 10, and HH 11, respectively. In these composites, the I-band image (F814W; red) shows primarily continuum sources such as stars and reflection nebulae, although HH objects also radiate several weak emission lines (e.g. [Ca II] λ7291, [O II] $\lambda\lambda$7321+7330, [Ni II] λ7380, [Fe II] λ8617, etc.) within this bandpass. The Hα (F656N; FWHM $\sim$ 18Å), [O I] λ6300 (F631N; FWHM $\sim$ 61Å) and [S II] λ6716 (FQ672N; FWHM $\sim$ 19Å) filters isolate single emission lines. Only relatively bright stars have enough continuum to be detected in these filters. None of the HH objects in the field have a detectable continuum component in the F645N filter (FWHM $\sim$ 85Å). Continuum is sometimes present in the I-band images of the HH objects because the I-band is less affected by reddening than the R-band, and because the bandpass of the F814W filter ($\sim$ 2000Å) is much wider than those of the narrowband filters.

Because the HH objects in HH 7-11 are pure emission-line sources, we can create difference images and emission ratio maps directly from the zero-point-corrected Hα, [O I] λ6300 and [S II] λ6716 images. As noted in Sec. 1, [O I] λ6300 and [S II] λ6716 trace similar regions in the cooling zones of shocks, while the surface brightness of Hα peaks in a narrow shell immediately behind the shock for low-velocity shocks like those in HH 7-11 (e.g. Hartigan & Wright 2015). Hence, the difference image Hα − ([O I] λ6300 + [S II] λ6716) can be useful for separating shock fronts from their cooling zones. Shocks should become manifest in the subtraction images as filamentary Hα-bright structures.

Two line ratio maps are particularly useful as diagnostics in HH 7-11. The first of these, [O I] λ6300 / [S II] λ6716, is normally not a particularly good density diagnostic because its value depends linearly upon the ionization fraction of O in the cooling zone, a quantity that is affected both by the preshock ionization fraction and by the shock velocity. However, the shocked regions in the HH 7 - 11 outflow are special cases in that they have unusually low-excitation optical spectra, such as [N II] λ6583 / [N I] λ5198+5200 $\lesssim$ 0.1, [O I] λ6300 / Hα $>$ 1 and [S II] λ6716 / Hα $>$ 1, weak [O II], and no [O III] lines (Böhm et al. 1983; Solf & Böhm 1990). These ratios all imply very low H-ionization fractions of at most a few percent. The ionization fraction of oxygen is tied to that of hydrogen through strong charge-exchange reactions (Williams 1973), so the ionization fraction of oxygen is also at most a few percent in low-excitation HH objects. Ionization effects are unimportant for S; the low ionization threshold of S implies it should be at least singly-ionized throughout the cooling zone, and the lack of any [S III] lines implies that all S is S II to within a few percent.

Under these mostly neutral conditions, [O I] λ6300 / [S II] λ6716 becomes an excellent diagnostic of relative density throughout the flow. In fact, the [O I] / [S II] ratio is superior to the standard [S II] λ6716 / [S II] λ6731 ratio in that it can measure electron densities

two orders of magnitude above the high density limit ($\sim 2 \times 10^4$ cm^{-3}) of the [S II] ratio. The [O I] λ6300 / [S II] λ6716 ratio increases monotonically with electron density because the critical density of [O I] λ6300 is much higher than that of [S II] λ6716. The temperature dependence in the [O I] λ6300 / [S II] λ6716 line ratio is weak, and a recent large grid of shock models shows that S II and O I emit at similar temperatures in the postshock region ($\sim$ 8000 K; Hartigan & Wright 2015).

We must scale [O I] λ6300 / [S II] λ6716 by the abundance ratio of O and S to use it to calculate electron densities quantitatively, though the relative densities across a given map are unaffected by this normalization constant. In the HH 7-11 region we can determine the O / S abundance ratio by combining our data with published ground-based spectra. The observed [S II]λ6716 / [S II]λ6731 ratio in a 6.9 arcsecond aperture centered on HH 11 is 0.82 (Böhm et al. 1983; Solf & Böhm 1990), implying log(N$_e$) = 3.06 using modern values of collision strengths (Shaw & Dufour 1994) for T $\sim$ 8000 K. For temperatures between 7000 K and 9000 K characteristic of shocked cooling zones, ionization fractions between 0 and 0.1, and an O / S gas abundance ratio of 35 (log O = 8.87, log S = 7.33 with log H = 12) the [O I] λ6300 / [S II] λ6716 ratio in a 5-level atom calculation for N$_e$ = 10^3 cm^{-3} gives 0.71, with a scatter of $\pm$ 15%.

The observed ratio of [O I] λ6300 / [S II] λ6716 in our HST images over the same region is 0.58 $\pm$ 0.08. Dereddening this ratio with E(B$-$V) = 0.62 (Böhm et al. 1983, corresponding to $C_{H\beta}$ = 0.98), we get [O I] λ6300 / [S II] λ6716 = 0.65 $\pm$ 0.08 for HH 11, in agreement with the value of 0.71 expected from the observed electron densities. The same procedure using the ground-based spectra of HH 7 (Solf & Böhm 1990) gives similar agreement. Hence, our observations are consistent with a normal abundance ratio for O / S in the HH 7-11 region.

Diagnostic curves for the [O I] λ6300 / [S II] λ6716 emission line ratio are shown in

Fig. 5 for three temperatures, assuming neutral O, singly-ionized S, and an O / S abundance ratio of 35. As a check, the observed ratios throughout the image fall within the allowed range for these abundances, and indicate electron densities that range from the low density limit ($\lesssim 100$ cm^{-3}) to $\sim 2 \times 10^4$ cm^{-3} (Fig. 5).

The Hα / [O I] λ6300 ratio is another important line ratio we can measure directly from our images. Böhm et al. (1983) noted that both HH 7 and HH 11 had unusually low-excitation spectra for HH objects, with Hα / [O I]λ6300 $\lesssim 1$. Integrated over the entire object, a lower value for Hα / [O I]λ6300 implies a lower shock velocity (Fig. 8 of Hartigan et al. 1994), and this constraint together with the other observed line ratios implies shock velocities $V_S \sim 30$ km s^{-1} according to the diagnostic curves of (Dopita & Sutherland 2017, cf. their Fig. 5). For images like ours where the cooling zones are resolved spatially, a lower value of Hα / [O I]λ6300 signifies the location of the T $\sim$ 8000 K gas.

Background-corrected ratio images for [O I] λ6300 / [S II] λ6716 and for [O I] / Hα appear in Figs. 2, 3, and 4 along with multicolor composites that employ the same color schemes as in Fig. 1. The ratio images exclude points, shown as grey, where the count rate is lower than a threshold in either the numerator or the denominator. We chose threshholds of 0.0035, 0.0030 and 0.0030 electrons/second for [O I], [S II], and Hα, respectively, because they produced ratio images with minimal scatter while still spanning each of the HH objects in the field.

3.1. HH 7

Fig 2 shows that the three brightest components of HH 7, labeled A, B, and C in the Figure, each have an overall bow-shape characteristic of a flow moving from WNW to ESE. A narrow outer rim visible only in the I-band precedes knot A, while a similar inner rim

defines the eastern edge of the Hα and forbidden line emission in this object. None of the other HH objects show similar rims in the I-band. The I-band rim has no counterpart in the images of the bright red emission lines of [O I], [S II] and Hα. Hence, this feature must emit mostly continuum, and in star formation regions this typically occurs along the walls of a cavity that reflects the light of a nearby protostar. The H_2 emission here is also unique for the region, appearing as a sharp arc that follows along the I-band rims. Unfortunately, the resolution of the ground-based H_2 is too low to determine any spatial offsets between the H_2 and I-band rims. The I-band and H_2 rims likely mark the terminus of the flow, with the I-band rim arising mostly from light reflected from shells of dust at the end of the cavity, while the H_2 could come from a precursor to the optical shock in knot A. This area has great potential for elucidating the physics of molecular shock waves, and should be a prime target for future study with JWST.

The brightest portion of HH 7A is located about one arcsecond to its west of the inner rim, and has a complex, serrated morphology anchored by a bright knot at its northern end (Fig. 6). A complex region of emission situated inside of a bow shock like this is expected of a working surface, where jet material decelerates. The brightest knot splits into three components upon close inspection and appears to have a wake to the southwest, mainly visible in Hα. The knot stands out as the region of highest electron density ($\gtrsim 10^4$ cm^{-3}) in the [O I] / [S II] ratio map, and also has a relatively low Hα / [O I] ratio. The knot also radiates in the I-band, but as this part of the spectrum also emits forbidden lines we cannot tell what fraction of the I-band emission in this object arises from lines and what fraction comes from continuum.

Like HH 7A, HH 7B also has a bow-shape, and it is possible to trace the wings of the bow shock in Hα $\sim$ 5 arcseconds to the north of the object, as well as $\sim$ 5 arcseconds to the southwest, where it overlaps with HH 7D at the edge of the flow. These Hα wings are

easiest to follow in the difference image in the lower right panel of Fig. 2. HH 7B has two bright Hα knots of diameter $\sim$ 0.3 arcseconds that show up well in the difference image. The inner bow HH 7C is less-distinct, but has the same overall appearance as HH 7B.

3.2. HH 8

The emission line images of Hα, [S II] and [O I] reveal HH 8 to be a remarkable object that consists of two distinct loops, (denoted A and B), situated above a bright linear feature (knots C and D; Fig 3). The periphery of knot A breaks up into multiple knots, the brightest and densest of which occurs where loop A intersects with loop B. On small scales, knot C breaks into two components and knot D into three, the easternmost of the three showing distinctly higher [O I] / [S II] than the other two. The H_2 contours peak between knots C and D. The forbidden-line emission is much weaker compared with Hα in HH 8 than it is in HH 7, so the difference image of HH 8 is not particularly illustrative. The I-band image shows what appears to be an extended background nebula, probably the rear wall of a cavity evacuated by the jet. A distinct dark lane cuts across this nebula, but does not seem to affect HH 8B, as expected if the HH object lies above the obscuring lane and the background nebula.

3.3. HH 9

HH 9 is a rather indistinct source located along the northeastern edge of the cavity defined by the reflected light in the I-band image (red in Fig. 1). It has a diameter of just over an arcsecond, and has little substructure. The HH object is visible in Hα and [S II] λ6716, and also detected faintly in [O I] λ6300.

3.4. HH 10

Like HH 8, HH 10 has a remarkable, nearly rectangular loop (HH 10B) located north of bright knots of emission (HH 10A and HH 10C; Fig. 4). Like HH 8A, the HH 10B loop breaks up into multiple knots, including one knot that emits strongly in Hα and in [O I] relative to [S II] (a blue-green dot in the upper left panel and white dot in the lower right panel). The densities are on average higher along the west side of HH 10 and lower along the east side. Knot A is notable in that it has the strongest forbidden lines relative to Hα. Diffuse H_2 emission spans the extent of HH 10.

3.5. HH 11

HH 11 is the highest-excitation object in the chain, with the strongest Hα emission relative to [O I] and [S II]. The Hα separates into two distinct objects, HH 11A, a tadpole-shaped feature located closer to the driving source, and HH 11B, a shell-like object that precedes HH 11A in the flow. Forbidden lines are essentially absent in HH 11B, and only weakly present in HH 11A. There is no H_2 emission, and the I-band shows only faint features as one would expect from weak emission lines in the band. Both HH 11 and HH 10 are located in a hole in the reflected-light cavity seen in the I-band (Fig. 1).

4. Distances and Resolved Young Stellar Objects in the Field

The NGC 1333 region contains 205 candidate young stellar objects according to a recent survey (Foster et al. 2015, see also Rebull (2015)), and 14 of these are visible in our images. The candidate young stars are all 2MASS infrared sources, and most have designations from previous near-IR catalogs (e.g. Aspin et al. 1994, sources designated as ASR). There are several molecular outflows and H_2 jets within NGC 1333 (Plunkett et al.

2013; Garden et al. 1990).

Figure 7 displays a histogram of the distances determined by GAIA-2 catalog for members of NGC 1333 (Gaia Collaboration 2016, 2018). Of the 205 sources in Foster et al. (2015), 114 were detected by GAIA, 99 had parallax measurements, and 50 of these had parallax errors $< 10\%$. Using 10000 bootstrap samples, the median value for the distance is 296 ± 5 pc. This distance is consistent with previous estimates based on Hipparchos data (de Zeeuw et al. 1999; Belikov et al. 2002). In this paper we adopt 300 pc as the distance to the HH 7-11 outflow.

A large-scale imaging survey of this region with HST in the near-IR taken nearly simultaneously with our observations (GO 15153; D. Watson PI) will investigate the stellar objects in more detail. However, a few of the young stars have resolved circumstellar nebulae in our images that warrant discussion here. SVS 13A shows the most interesting morphology of the young stars in our images (Fig. 8). The I-band reveals at least three arc-shaped nebulosities, leaving the impression of two elliptical-shaped cavities that originate from SVS 13A. The smaller cavity has PA = 162 ± 2 degrees and major axis 1.9 ± 0.1 arcseconds, and the larger one PA = 156 ± 2 degrees with major axis 2.8 ± 0.1 arcseconds. The sizes of the minor axes are 1.0 and 1.6 arcseconds, respectively. These cavities correspond with those observed in H_2 by Hodapp & Chini (2014), who also observed a third, smaller cavity close to the source. These observations imply a scenario where multiple ejections driven from SVS 13A in a southeasterly direction leave behind fossil cavities.

The [O I] λ6300 and [S II] λ6716 images show that a microjet extends ~ 0.3 arcseconds to the southeast of SVS 13A at PA = 145 degrees, in the general direction of the HH 7-11 outflow. This jet is also seen in Fe II 1.64μm AO datacubes taken with Keck (Hodapp & Chini 2014), where the radial velocity of ~ -140 km s^{-1} shows some evidence for variability.

SVS 13A itself is clearly variable between the two HST epochs, having faded by 0.37 ± 0.1 magnitudes between 1998 and 2018 in the Hα images when compared with the two nearby bright stars ASA 2 and ASA 3 (all unsaturated in the narrowband images). The decline in brightness is similar, 0.39 mag, in the narrowband O I filter.

Our HST images also show extended arcuate nebulosities typical of evacuated cavities and embedded objects around two stars to the northeast of SVS 13A (Figs. 1, 8). The I-band images of the first of these, ASR 7, shows a broad arc centered on the source and extending several arcseconds to the west. The nebula is significantly brighter on its north side than its south side. ASR 7 (2MASS J03290575+3116396) is an X-ray source and has very red colors in the near-IR (K $\sim$ 10, J$-$K $\sim$ 4.5; Winston et al. 2010). Spectra reveal a rapidly rotating early M/late-K star, with a significant amount of veiling at H (Foster et al. 2015). Two fainter stars noted by Oasa et al. (2008) are visible in our images as well, situated about 2 arcseconds to the NE and to the SE of ASR 7. The other star in this region with a circumstellar nebula in our images is ASR 105. This nebula has a compact C-shape that extends $\sim$ 1 arcsecond to the northeast of the source. ASR 105 lies near the brown dwarf limit, with a spectral type of M6 and a signficant veiling in the near-IR indicative of ongoing accretion (Greissl et al. 2007).

Finally, ASR 2 (2MASS J03290289+3116010), located $\sim$ 11.5 arcseconds to the WSW of SVS 13A, resolves cleanly into a close binary in our HST images in Fig. 8. Using DAOPHOT, we find the secondary is positioned nearly due north of the primary at PA=0.8 ± 2.1 degrees, separation = 0.15 ± 0.01 arcseconds, with a magnitude difference of 0.98 ± 0.07 relative to the primary in the R-band continuum image. We used the other nearby bright star, ASR 3 (2MASS J03290216+3116114), as the point-spread-function star for the photometric and positional measurements. The secondary of ASR 2 is distinct in all the different filters, though is more difficult to see in the I-band image because the primary is

saturated in those exposures. Foster et al. (2015) characterized the combined spectrum of both components of ASR 2 as a slowly-rotating, weakly-veiled T-Tauri star with an effective temperature of 3760 K and a radial velocity consistent with membership in NGC 1333. We checked to see if any orbital motion might have occurred between our observations and those of the previous HST images taken in 1995 and 1998, but the binary nature of ASR 3 was unclear in the archival WFPC2 images owing to the larger pixel sizes in those data. This object would be a good one to monitor in the future for orbital motion as a means to test the pre-main-sequence evolutionary tracks for very low mass stars.

5. Proper Motions and Variability of the HH Objects

The HH 7-11 outflow has been targeted for narrowband optical imaging with WFPC2 on HST in two previous campaigns. In 1995, program GTO-5779 observed the region in Hα (F656N), [S II] (F672N), and I-band (F850LP), but a positioning error left all of HH 7 outside the field of view. Just over three years later, GO-6868 observed the same region in Hα (F656N), [S II] (F672N), and [O I] (F631N), but these observations again missed the tip of the bow shock in HH 7. However, both sets of observations imaged HH 8, HH 9, HH 10, and HH 11, so we can combine the previous images with ours to measure high-precision proper motions for these objects. It is possible to measure proper motions for some interior portions of the HH 7 bow shock from GO-6868, but not for the apex. No proper motions are evident in the three year time-interval between the GTO-5779 and GO-6868 images of HH 8, HH 9, and HH 10. These images are similar enough that we combined them into a single epoch to increase the signal-to-noise. A proper motion of a few pixels directed away from SVS 13 is present between GTO-5779 and GO-6868 in HH 11.

Images in GTO-5779 and GO-6868 (both referred to here as epoch 1) were not dithered when acquired, and so have somewhat poorer spatial resolution than we achieve in our

current (epoch 2) dataset. This effect slightly blurs the epoch 1 data relative to epoch 2 but does not affect the proper motion measurements. Alignment between the three datasets is a more difficult issue. The bright stars SVS 13, ASR 2, and ASR 3 are present in all the images, but the field does not have any visible stars to the southeast in the vicinity of HH 7. Moreover, SVS 13 has a variable microjet in Hα and [S II] that affects its photocenter (Fig. 8), while ASR 2 is a binary (Sec. 4; Fig. 8) and is saturated in most exposures. A few stars are available for alignment to the north and west of SVS 13, but these are out of the field of view for some of the observations, and faint in the narrowband filters. For these reasons we used the orientation and pixel scale recorded when the observations were taken to rotate and scale the images, and relied upon the HST reduction pipeline to correct for spatial distortion. After rotation and scaling, the zero-points of the world-coordinate systems aligned to within an arcsecond or so, and we did a final spatial shift to align the photocenter of ASR 3 in each image. The resulting alignments should be accurate to within 1 WFPC2 pixel (0.1 arcseconds), and may be better than that, but we cannot confirm this owing to the lack of alignment stars.

The epoch 1 and epoch 2 images in Hα are presented side-by-side in Fig. 9. We measured proper motions for the regions indicated in each of the light-blue boxes. Each figure also shows several white boxes, which we present as fiducials that aid in viewing the motions between epochs. If the reader expands the images to a comfortable size and then looks quickly between the left and right panels, it should become clear both how the emission translates in bulk relative to the fixed white and blue boxes, and the degree to which the objects vary morphologically in the 20-year timespan between the epochs. The reader may also refer to the on-line animated figure, which switches back and forth between the epochs for HH 7 and HH 8 (Fig. 10) and for HH 10 and HH 11 (Fig. 11).

5.1. HH 7

Our proper motion measurements in HH 7 are limited because both epoch 1 images omit its most recognizable feature, the leading bow shock. Nevertheless, a few filamentary structures that follow in the wake of the main bow shock retain enough of a coherent morphology to be useful for proper motion measurements. The four areas shown in Fig. 9 have small, but nonzero proper motions to the east, as suggested by the orientation of the leading bow shock. The fastest object is the arc-shaped bow HH 7C, at 38 $\mathrm{km\,s^{-1}}$, with the slowest being HH 7E, at 12 $\mathrm{km\,s^{-1}}$. Small proper motions in declination are near the limit of confusion with morphological changes in the shocked gas.

5.2. HH 8

Emission within the blue rectangle that defines the extent of HH 8 in Fig. 9 exhibits no detectable proper motion ($\lesssim$ 6 $\mathrm{km\,s^{-1}}$, Table 1). However, HH 8 shows remarkable structural changes between the two epochs. Both loops HH 8A and HH 8B expand noticeably in the 20-year interval, HH 8A by 25 ± 5 $\mathrm{km\,s^{-1}}$ along its northern and southern portions, and HH 8B by about half this speed along its western side. The interface between the two loops is stationary. The bright knots HH 8C and HH 8D located to the southeast of the two loops have no bulk proper motions, but their relative brightnesses have changed, with knot HH 8C brighter than knot HH 8D in the late 1990's and knot HH 8D the brighter of the two now. HH 8D is notable for its current strong forbidden line emission and high electron density, particularly along its eastern edge (Fig. 3). The sharp Hα filament to the north of HH 8A is now more diffuse.

5.3. HH 9

Figure 1 shows HH 9 to be an indistinct source situated along the edge of a cavity outlined by the reflected light present in the I-band. The source is a diffuse structure that shows no significant proper motions or morphological changes.

5.4. HH 10

Like HH 8, HH 10 has no bulk proper motion ($\lesssim 6$ km s^{-1}), but exhibits structural variability. The large loop HH 10B retains its overall shape between the epochs, but several small clumps have now appeared on both the east and west sides of the loop. One compact knot has largely replaced the three elongated ones that defined the northwestern corner in the epoch 1 image. At the base of the loop, the three knots that make up HH 10A have been replaced by a single knot. One gets a general impression that the large loop HH 10B has become narrower shifted a bit along the direction of the flow. This impression is driven largely by the appearance of the western side of HH 10, which curves to the west in epoch 1 but becomes more straight in epoch 2.

5.5. HH 11

HH 11 has by far the highest proper motions in the region, ~ 1.2 arcseconds over the ~ 20 year time interval. Motion is directed away from SVS 13. Morphological changes in HH 11 are rather minor. The leading shell of Hα separates from the trailing blob of Hα and forbidden line emission by $\sim 0.3''$ in the new images, somewhat more than in the epoch 1 data where there is no clear space between these components. But otherwise, HH 11 retains its shape well over the period.

However, HH 11 is noticably fainter in the most recent epoch relative to the other HH objects. All the HH objects appear brighter by $\sim 30\%$ *relative to the stars* in the second epoch Hα images, but this increase simply results from the narrower bandpass of the F656N filter in the WFC3 images relative to the WFPC2 images (the effect is reversed in F631N, where WFC3 has the broader bandpass). However, flux differences between HH objects *are* significant because even the narrowest WFC3 bandpasses include all the emission from HH 11, the most blueshifted object. For example, the transmission curve for F656N in WFC3 drops off only when velocities are more blueshifted than ~ -450 km s^{-1}, a factor of two higher than the most blueshifted emission from HH 11. We find that the Hα flux from HH 11 has declined by $36\% \pm 10\%$ in the 20 years between the epochs. The decline in [O I] is even greater, $50\% \pm 10\%$.

6. Discussion

6.1. Orientations, Deflections, Mass Loss Rates, and The Rings of HH 8 and HH 10

It has been standard practice in the field to infer the orientation angle of jets relative to the line of sight by simply combining proper motion and radial velocity measurements, and this procedure works well as long as the HH object behaves like a bullet that propagates through the surrounding medium. However, the emission in HH 8 and HH 10 arises from loop-shaped structures that have no substantial proper motions, yet exhibit significant radial velocities and line widths ($\sim 50-70$ km s^{-1}; Solf & Böhm 1987). A simple way to explain these observations is to have the shocked gas arise along an interface where the jet has pierced through or has been deflected from a sheet of ambient material. In such a scenario, jet material is continuously shocked and possibly redirected at these interfaces. The interfaces will not exhibit any bulk motion because they are fixed to the sheet of

material, and any expansion of the rings results from the expansion of the shock within the sheet.

(Raga et al. 1996) modeled the passage of a jet through a clumpy medium, and identified HH 7-11 as a possible example of such a flow, a conclusion now strongly supported with the new Hubble images. The numerical models show that clumpy media produce a variety of morphologically complex time-dependent shock waves as the jet deflects from clumps and the clump shapes become modified by shock waves. In general, shocks in the clumps have small proper motions, as observed. No loops like we observe in HH 8 and HH 10 are obvious in the simulations, but these could very well appear in higher spatial resolution models or with different sets of initial conditions for the clump densities and geometries. Situations where jets interact with clumps should be common, as jets often extend for parsecs (Reipurth et al. 1997) and far-IR images reveal many complex filamentary structures in star forming regions, including NGC 1333 (Dhabal et al. 2018).

The shocks in HH 8 and HH 10 appear to be redirecting the outflow. Together, HH 11, HH 10, HH 8, and HH 7 outline a flow that is initially oriented to the southeast, but points almost due east by the time the flow reaches HH 7 (Fig. 12). The southern edges of the rings HH 8D and HH 10A, have low-excitation (high [O I] / Hα) spectra and also emit in H_2, implying a dense layer along that side, exactly what is needed to deflect the jet in the observed direction (Figs. 3, 4). The clumpy morphological changes in HH 8 and HH 10 make sense as transient phenomena that occur as the jet deflects from the obstacles. A reflection nebula with a remarkable curved dark lane associated with the loops in HH 8 in the I-band image (Figs. 1, 3) is further evidence for a stationary obstacle at this location.

HH 8 and HH 10 are good examples as to why *using line luminosities to infer mass-loss rates in jets can give erroneous results.* These HH objects are stationary, and emit only because the jet shocks material along its periphery. If the sheets weren't there, no emission

would occur and the line luminosities would be zero. In the current configuration, jet material that radiates in HH 10 and HH 8 will radiate again when it encounters HH 7 further down the flow, so in this case an atom in the flow will experience multiple heating and cooling events. Using luminosities to measure mass loss rates only makes sense if either (a) the jet measurements are close enough to the source where one might argue that the entire flow radiates before any material gets shock-heated and entrained, or (2) the emission only comes from bullets of ejected gas, and not from shocked ambient gas. However, the former case is sensitive to the beam size, as larger beams will include more emission, and the second scenario may not produce any observable emission, because only velocity differences produce shocks. A bullet could propagate along a jet and be invisible until it encounters slower material. Such a situation has been observed in HH 1, for example (Hartigan et al. 2011). The best scenario is probably one where the jet is resolved spatially, and densities and velocities can be measured close to the source before encounters with the surrounding medium complicate the situation.

6.2. HH 7, HH 11, SVS 13A, and the Nature of the Outflow

HH 7 appears to be the terminus of the outflow, as the HST images show no optical emission beyond HH 7 that would indicate a continuation of the flow. This conclusion is supported by the presence of a large H_2 bow shock in HH 7 (Fig. 2). There is also no optical emission from the redshifted side of the molecular flow, though the extinction there is undoubtedly large.

The HH 7 bow shock is arguably the best object in the sky for studying how molecular emission within C-shocks relates to its J-shock counterpart traced by optical lines. Figs. 2 and 6 reveal that the brightest portion of HH 7A has an unusual serrated appearance. We take this feature to be the working surface, where clumps in the jet decelerate as

they encounter the dense ambient cloud (see Fig. 6). The brightest knot splits into three smaller components down near the spatial resolution limit of the observations. These bright knots are trailed by what appears to be a wake. Apparently parts of the jet become small, bullet-like clumps before they decelerate in the HH 7 working surface. The wavy morphology of the working surface could give rise to Mach stems where curved shocks intersect (Hartigan et al. 2016), although any such structures would be unresolved in these data. The feature marked as 'Inner Rim' seems to mark the edge leading bow shock, as it encloses the extent of the Hα and forbidden line emission. Unfortunately proper motion measurements are not yet available for this region owing to the pointing errors in the early HST images. Interestingly, our I-band image also shows that an 'Outer Rim' cavity extends to the east beyond the forbidden line emission. How this cavity relates to the H_2 emission is unclear, as existing ground-based H_2 images do not locate the molecular gas with enough precision.

Because they represent distinct structures of moving gas, we can use both HH 7C and HH 11 to measure flow velocities, orientation angles, and dynamical ages for these objects. Emission from HH 7 occurs primarily along a series of three nested arcs that resemble bow shocks, HH 7A, 7B, and 7C (Sec. 3), and we have proper motion measurements for HH 7C (Table 1). Combining this measurement with the observed radial velocity at this location of -82 km s^{-1} with respect to the molecular cloud (Solf & Böhm 1987), we obtain a flow velocity of 90 km s^{-1} and an orientation angle of 25 $\pm$ 5 degrees from the line of sight for HH 7C. Similarly, using a radial velocity of -200 km s^{-1} for HH 11 we find a flow velocity of 220 km s^{-1}, and an orientation angle of 24 $\pm$ 2 degrees. However, even though their orientation angles to the line of sight are essentially the same, the velocity vectors of HH 11 and HH 7 are not parallel to one another because the jet is deflected to the east by HH 8 and HH 10 (see below). The dynamical ages are 2360 years and 285 years, respectively, for HH 7C and HH 11. Continuing on its current trajectory, HH 11 should overrun HH 10

around the year 2180, and produce a strong shock wave at that time.

Fig. 12 summarizes the proper motion results. The jet currently emerges with a space velocity of ~ 160 km s^{-1} at PA ~ 145 degrees. We take its orientation to the line of sight to be 24 degrees, the same as that of HH 11. Some 12,600 AU (5100 AU projected) along the jet we encounter HH 11, a bullet-like ejection with a velocity of 220 km s^{-1} and an inclination of 24 degrees. Its shock velocity is less than 90 km s^{-1} owing to the lack of [O III], but has a line width of ~ 70 km s^{-1} Solf & Böhm (1987). Taking this width as an indication of the shock velocity (Hartigan et al. 1987), the jet material ahead of HH 11 moves at ~ 150 km s^{-1} away from the source. The fading of HH 11 could arise from a lower density, or a faster preshock medium (lower shock velocity) in the second epoch relative to that of the first epoch.

The jet disappears between HH 11 and HH 7, where we see only the clumpy, variable stationary objects HH 8 and HH 10 as shocked knots along the flow's periphery. By the time we see clear evidence for jet material again in HH 7C, the orientation to the line of sight is essentially the same as it was for HH 11, *but the proper motion vector has shifted by about 55 degrees towards the east.* As depicted in Fig. 12, because the flow has a significant component towards the observer, a small deflection of the jet can produce a larger angular change in the proper motion vector. In this case, it is possible to change the proper motion vector orientation by 55 degrees by redirecting the jet ~ 23 degrees, something easy to do for a 150 km s^{-1} (Mach ~ 15) jet via an oblique shock. The only evidence that the jet continues to flow through HH 8 and HH 10 is that the radial velocities of these objects are substantially blueshifted ($\gtrsim 50$ km s^{-1}) relative to the cloud. Whether or not the jet forms a continuous stream, its velocity has declined to~ 90 km s^{-1} at HH 7C. At this point the jet seems to become more fragmentary, breaking into smaller clumps that enter the working surface as small bullets in HH 7A (Fig. 6).

The HH 7 bow shock could be more or less stationary, with a very slow shock propagating into the molecular gas, but we do not yet have proper motion data to test this idea. Given a typical evolutionary timescale of $10^5 - 10^6$ years for the protostar, it is highly unlikely that we happen to be observing this jet when it is only a few thousand years old. Instead, if the jet encounters a much denser molecular cloud it will pile up into the shell that defines HH 7. Unable to break out of this cocoon, the jet nevertheless creates a cavity and gradually drives a molecular flow along the periphery of this shell. Normally we think of stellar jets as being much denser than their surroundings and penetrating for large distances. However, the HH 7-11 outflow seems to be an exception to that rule. The available data indicate that the flow is very young and has yet to fully emerge from the molecular cloud core that created the driving source SVS 13A.

The forbidden line emission here all aligns nearly along the axis of a reflected-light cavity whose base is located at SVS 13A, itself an embedded IR source with a disk that drives a microjet down the middle of the cavity. These facts argue strongly that all of the line emission in HH 7-11 originates from a single outflow. However, a dark hole in the reflected light cavity surrounds HH 11 and HH 10 (Fig. 1) and this striking feature remains unexplained in the above scenario. We initially considered a model where HH 7 and HH 11 arose from different flows projected onto nearly the same line of sight, perhaps from the two components of the SVS 13 binary (Plunkett et al. 2013). This dual jet model could explain the dark hole by having the HH 11 jet oriented more towards the observer so it punches through the larger cavity created by the HH 7 jet. However, this model is not consistent with the proper motion measurements, which show similar inclinations for HH 7C and HH 11 relative to the observer. It is worth noting that this region does contain several outflows (e.g. Dionatos & Güdel 2017), including a second molecular flow detected at mm-wavelengths along the western edge of the HH 7-11 cavity (Lefévre et al. 2017). However, none of these other flows seem to affect the shocked optical emission in this region.

7. Summary

When combined with archival images taken 20 years ago, the new narrowband emission line images of the HH 7-11 stellar jet reported in this paper allow us to measure precise proper motions throughout the flow for the first time. Our program is also the first to use a quad filter on HST to isolate only [S II] λ6716, making it possible to measure electron densities and line excitations everywhere throughout the flow with spatial resolution of $\sim$ 20 AU. The new images also uncovered several reflection nebulae suggestive of disks and cavities around embedded yonug stars in the area, and resolved one such object as a subarcsecond binary.

The source of the HH 7-11 outflow is SVS 13A, which drives a jet down the axis of a reflected-light cavity centered on the HH objects. The images have uncovered a new morphological structure not seen clearly before in any HH jet - both HH 8 and HH 10 are variable, ring-like structures that have no bulk proper motions but the shocked gas has a significant radial velocity. In HH 8 the rings appear to be expanding, while the motions in HH 10 are more chaotic. We interpret these features to be locations where the jet deflects from an obstacle along its path. In this sense, the HH 7-11 jet is similar to HH 110, which also exhibits line emission as the jet deflects from an obstacle in the flow (Riera et al. 2003; Lopez et al. 2005; Hartigan et al. 2009). The two obvious bow shocks, HH 7 and HH 11, have similar orientation angles of $\sim$ 25 degrees to the line of sight. HH 11 appears as a typical HH bow shock with a substantial proper motion, and is fading with time, while HH 7 consists of multiple arcs and knots.

The HH 7 bow shock seems to mark the end of the flow, though no proper motions yet exist for the apex of this feature. A complex working surface defines the region where knots in the fragmentary jet decelerate. The bow shock in HH 7 also emits strongly in H_2, making it an ideal target to study how C-shocks connect to their J-shock counterparts.

Such a comparison requires requires high-spatial resolution observations of the shocked H_2 emission, a high priority for JWST once it becomes operational.

The presence of emission line structures that align with the jet but do not participate in the outflow reinforces the need for caution when attempting to convert line luminosities in jets to mass outflow rates. Any such attempts should carefully consider how entrained material and shocks within ambient gas affect the mass loss estimates. These estimates are likely be reliable only close to the source before multiple shock waves alter the geometry of the flow.

Support for Program number GO-15257 was provided by NASA through a grant from the Space Telescope Science Institute, which is operated by the Association of Universities for Research in Astronomy, Incorporated, under NASA contract NAS5-26555. This work has made use of data from the European Space Agency (ESA) mission Gaia (https://www.cosmos.esa.int/gaia), processed by the Gaia Data Processing and Analysis Consortium (DPAC, https://www.cosmos.esa.int/web/gaia/dpac/consortium). Funding for the DPAC has been provided by national institutions, in particular the institutions participating in the Gaia Multilateral Agreement.

REFERENCES

Anglada, G., Rodríguez, L.F., & Torrelles, J.M. 2000 ApJ 542, L123

Aspin, C., Sandell, G., & Russell, A.P.G. 1994, A&AS 106, 165

Belikov, A., Kharchenko, N., Piskunov, A., Schilbach, E., & Scholz, R.-D. 2002, A&A, 387, 117

Böhm, K.-H., Brugel, E.W., & Olmsted, E. 1983, A&A 125, 23

de Colle, F., del Burgo, C. & Raga, A.C. 2010 ApJ 721, 929

de Zeeuw, P.T., Hoogerwerf, R., Bruijne, J.H.J., Brown, A.G.A., & Blaauw, A. 1999, AJ 117, 354

Dhabal, A., Mundy, L.G., Rizzo, M.J., Storm, S., & Teuben, P. 2018, ApJ 853, 169

Dionatos, O., & Güdel, M. 2017, A&A 597, A64

Dopita, M. & Sutherland, R. 2017 ApJS 229, 35

Dressel, L. 2019, *Wide Field Camera 3 Instrument Handbook, Version 11.0*, (Baltimore: STScI)

Foster, J.B, et al. 2015, ApJ 799, 136

Frank, A. 2007, Ap&SS 307, 35

Frank, A. et al. in *Protostars and Planets VI*, H. Beuther, R.S. Klessen, C.P. Dullemond, & T.K. Henning eds.,(Tucson:U of A Press), p451

Gaia Collaboration, 2016, A&A 595, 1

Gaia Collaboration, 2018, A&A 616, 1

Garden R. P., Russell A. P. G. & Burton M. G. 1990, ApJ 354 232

Geballe, T., Burton, M.E., & Pike, R.E. 2017 ApJ 837, 83

Gennaro, M. et al. 2018, *WFC Data Handbook*, Version 4.0, (Baltimore:STScI)

Greissl, J., Meyer, M.R., Wilking, B.A., Fanetti, T., Schneider, G., Greene, T.P., & Young, E. 2007, AJ 133, 1321

Hartigan, P., Foster, J., Wilde, B., Coker, R., Rosen, P., Hansen, J., Blue, B., Williams, R., Carver, R., & Frank, A. 2009, ApJ 705, 1073

Hartigan, P., Frank, A., Foster, J.M., Wilde, B.H., Douglas, M., Rosen, P.A., Coker, R.F., Blue, B.E., & Hansen, J.F. 2011, ApJ 736, 29

Hartigan, P., Foster, J., Frank, A., et al. 2016, ApJ 823, 148

Hartigan, P. & Morse, J. 2007, ApJ 660, 426

Hartigan, P., Morse, J., & Raymond, J. 1994, ApJ 436, 125

Hartigan, P., Raymond, J., & Hartmann, L. 1987, ApJ 316, 323

Hartigan, P. & Wright, A. 2015, ApJ 811, 12

Heathcote, S., Morse, J., Hartigan, P., Reipurth, B., Schwartz, R.D., Bally, J., & Stone, J. 1996, AJ 112, 1141

Herbig, G. 1974, Lick Obs. Bull. No. 658

Herbig, G.H. & Jones, B.F. 1983, AJ 88, 1040

Hodapp, K.W., & Chini, R. 2014, ApJ 794, 169

Khanzadyan T., Smith M. D., Davis C. J., Gredel, R., Stanke, T., & Chrysostomou, A. 2003, MNRAS 338 57

Lefévre, C., Cabrit, S., Maury, A.J. et al. 2017, A&A 604, L1

Lopez, R., Estalella, R., Raga, A., Reira, A., Reipurth, B., & Heathcote, S. 2005, A&A, 432, 567

Lucas, P.W., Hoare, M.G., Longmore, A.C., et al. 2008, MNRAS 391, 136

Nolan, C. A., Salmeron, R., Federrath, C., Bicknell, G. V., & Sutherland, R. S. 2017, MNRAS 471, 1488

Noreiega-Crespo A., & Garnavich, P.M. 2001 AJ 122, 3317

Oasa, Y., Tamura, M., Sunada, K., & Sugitani, K. 2008, AJ 136, 1372

Pike, R.E., Geballe, T.R., Burton, M.G., & Chrysostomou, A. 2016, ApJ 822, 82

Plunkett, A.L., Arce, H.G., Corder, S.A., Mardones, D., Sargent, A.I., & Schnee, S.L. 2013, ApJ 774, 22

Raga, A.C, Canto, J., & Steffen, W. 1996, QJRAS 37, 493

Raga, A.C, Reipurth, B., Velázquez, P.F., Esquivel, A., & Bally, J. 2016, AJ 152, 186

Raga, A.C, Noriega-Crespo, A., Carey, S.J., & Arce, H. 2012, AJ 145, 28

Riera, A., Raga, A., Reipurth, B., Amram, P., Boulesteix, J., Canto, J., & Toledano, O. 2003, AJ, 126, 327

Rebull, L. 2015, AJ 150, 17

Reipurth, B., Bally, J., & Devine, D. 1997, AJ 114, 2708

Romero, G.E., Boettcher, M., Markoff, S., & Tavecchio, F. 2017, Sp.Sci.Rev. 207, 5

Snell, R. & Edwards, S. 1981, ApJ 251, 103

Solf, J., & Böhm, K.-H. 1987, AJ 93, 1172

Solf, J., & Böhm, K.-H. 1990, ApJ 348, 297

Shaw, R.A. & Dufour, R. 1994, ASPC 61, 327

Strom, S.E., Vrba, F.J., & Strom, K.M. 1976, AJ 81, 314

Williams, R.E. 1973, MNRAS 164, 111

Winston, E., Megeath, S.T., Wolk, S.J. et al. 2010, AJ 140, 266

Yuan, Y., & Neufeld, D.A. 2011, ApJ 726, 76

Yuan, Y., Neufeld, D.A., Sonnentrucker, P., Melnick, G.J., & Watson, D.M. 2012, ApJ 753, 126

Zanni, C., & Ferreira, J. 2013, A&A 550, 99

This manuscript was prepared with the AAS LaTeX macros v5.2.

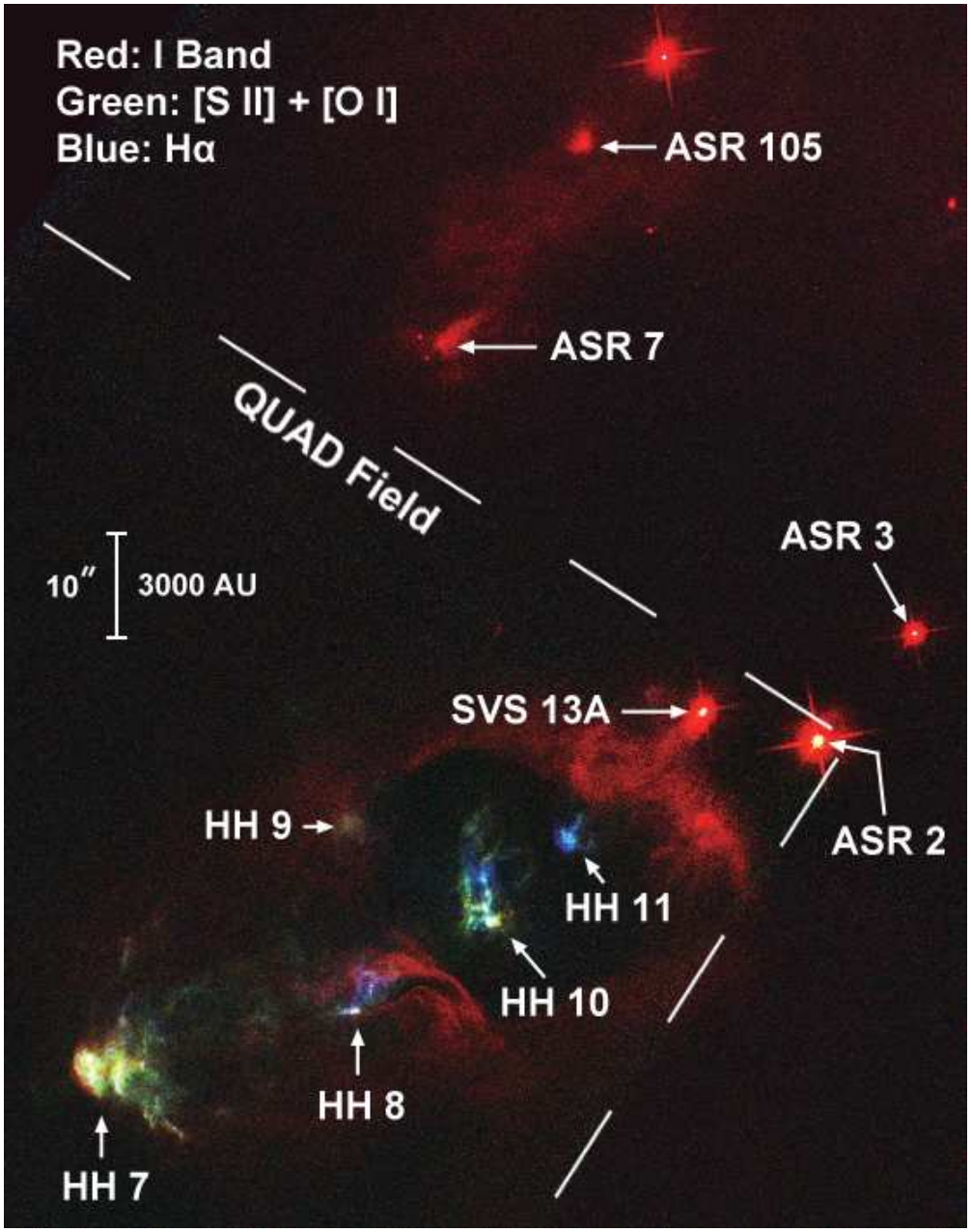


Fig. 1.— Color composite of the HH 7-11 Region from I-band (F850LP, a Sloan z′ filter; red), [S II] λ6716 + [O I] λ6300 (FQ672N + F631N; green), and Hα (F656N; blue) HST ACS images. The dashed region marks the boundaries of the [S II] QUAD filter. The HH objects and point sources discussed in the text are labeled. SVS 13A is the driving source of the HH 7-11 flow. North is up and east to the left.

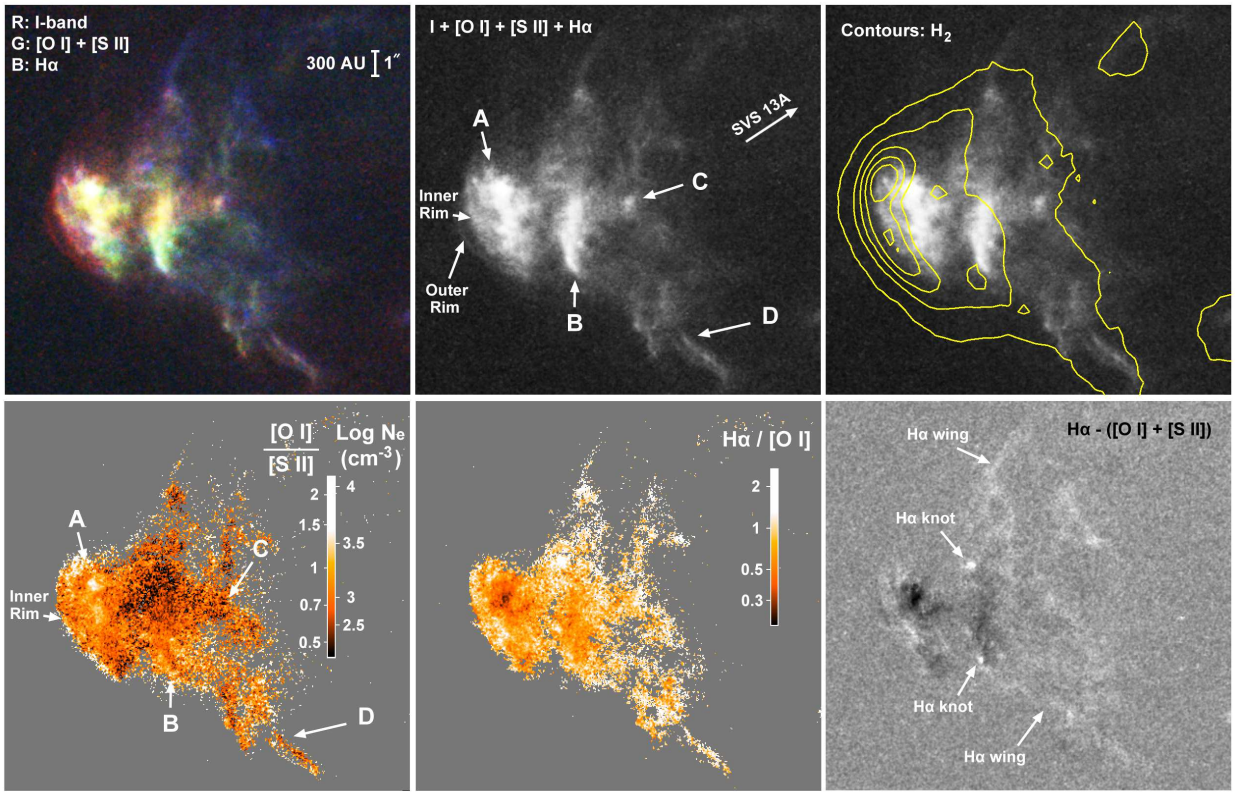


Fig. 2.— Top-left: Color composite of HH 7, with the I-band image (F850LP) in red, [O I]λ6300 + [S II]λ6716 (F631N+FQ672N) in green, and Hα (F656N) in blue. North is up and east to the left. The scale bar adopts a distance of 300 pc. Top-middle: Combined I + [O I]6300 + [S II]6716 + Hα image with the labeled features discussed further in the text. The direction to the exciting source SVS 13A is shown. Top-right: Contoured ground-based H_2 image superposed upon the HST optical emission. Bottom-left: The [O I] λ6300 / [S II] λ6716 ratio images, and their translations to log N_e using the 8000 K curve in Fig.5. Grey areas have low emission line fluxes in one or both lines. Bottom-middle: A similar ratio map for the Hα / [O I] λ6300 ratio. Bottom-right: A difference image between Hα (white) and the cooling zone forbidden line emission ([O I] + [S II], black).

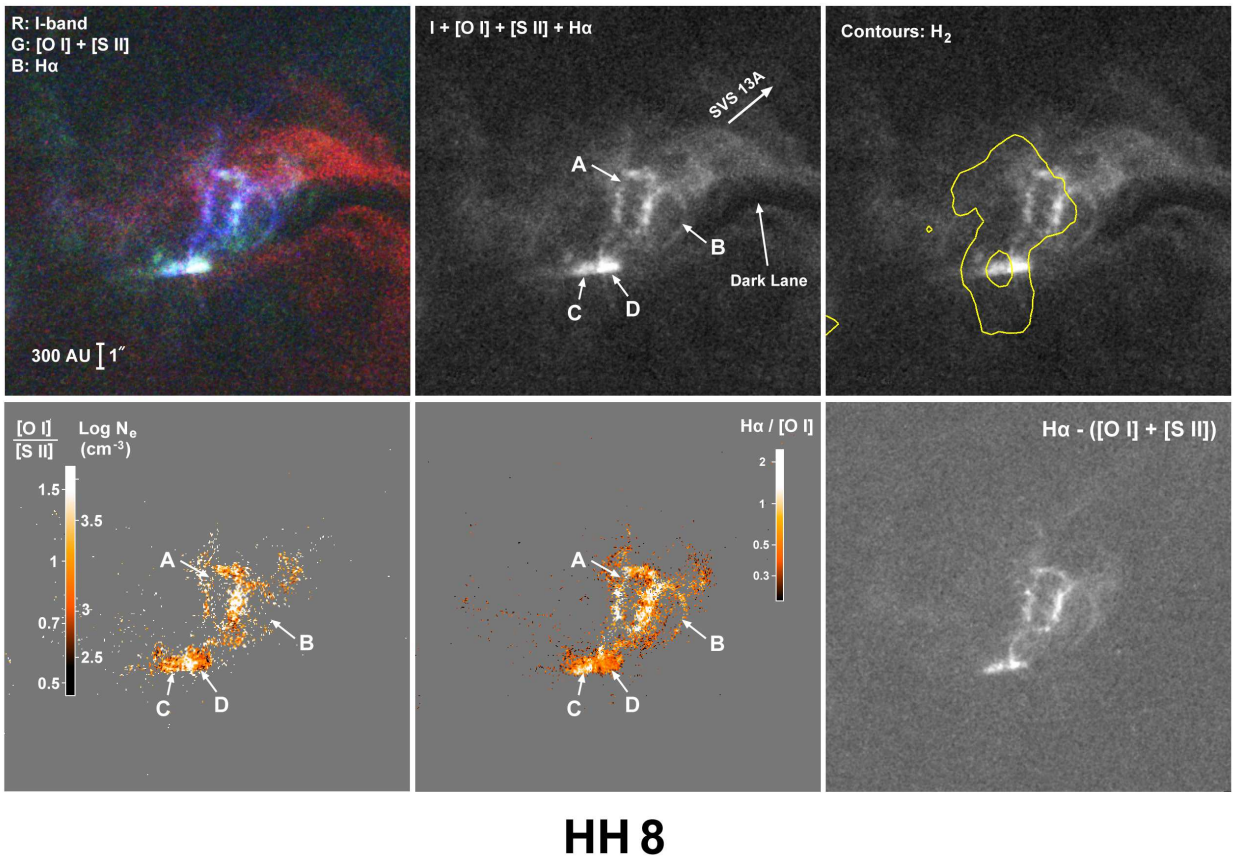
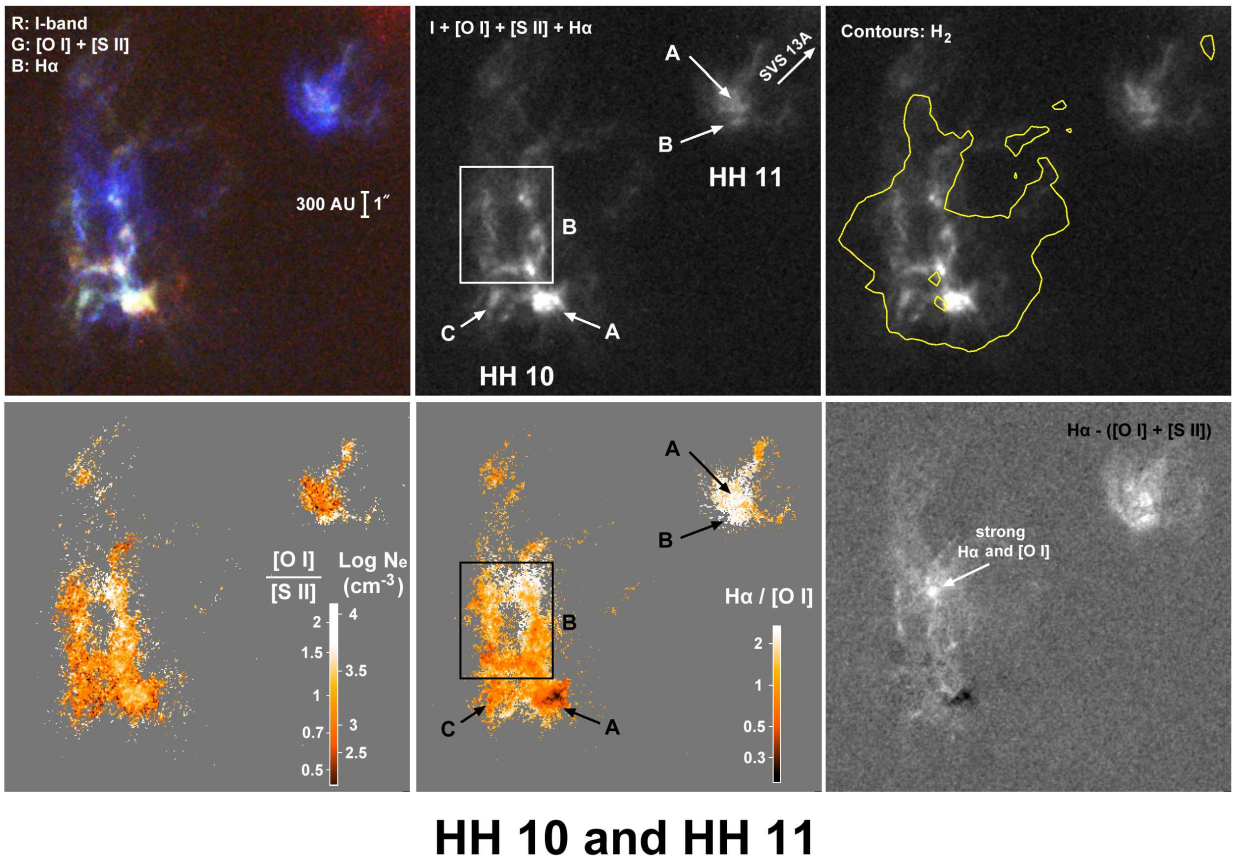


Fig. 3.— Same as Fig. 2 for HH 8.



HH 10 and HH 11

Fig. 4.— Same as Fig. 2 for HH 10 and HH 11.

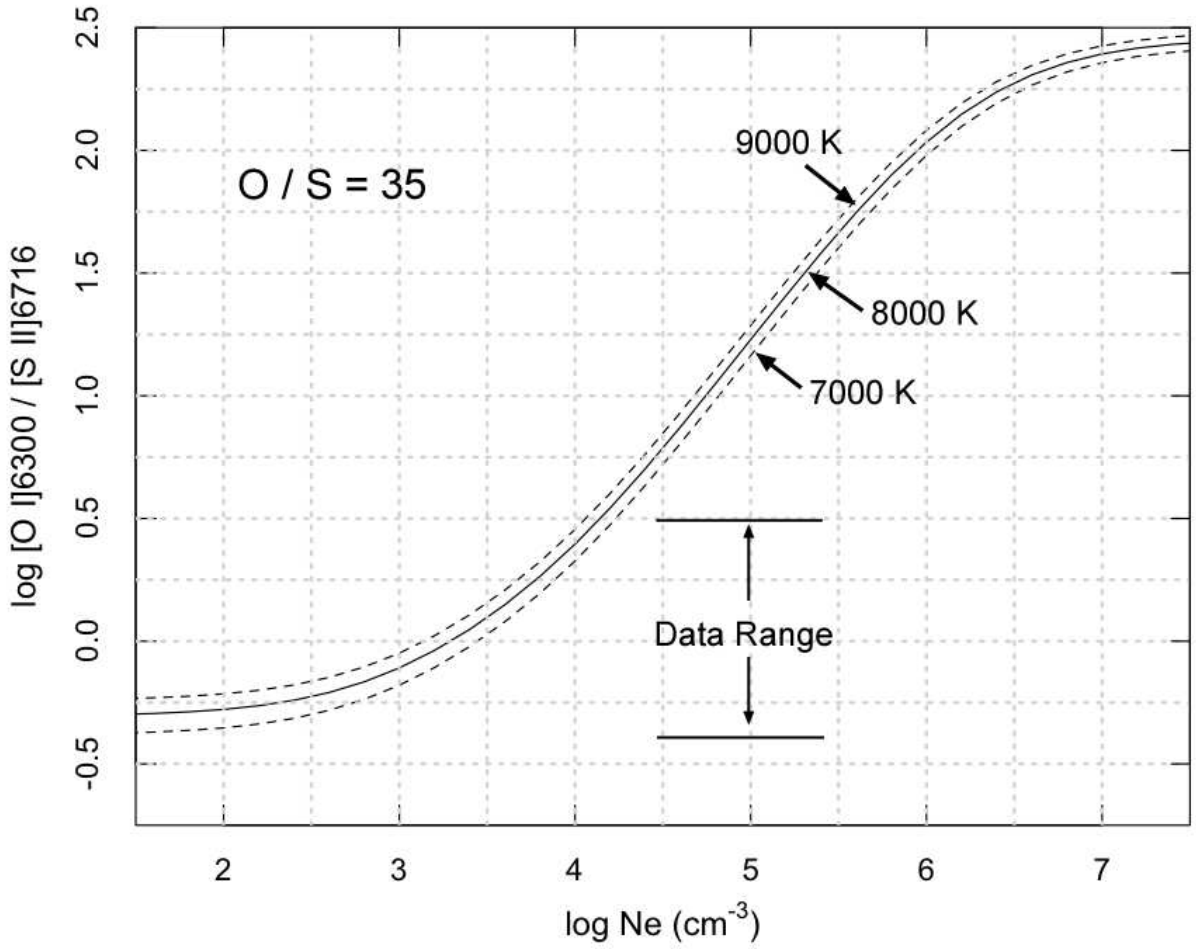


Fig. 5.— Diagnostic diagram for the [O I] λ6300 / [S II] λ6716 line ratio for three temperatures and an abundance ratio O / S = 35. The curves rise monotonically with density. The range of the ratio measured in the images is shown.

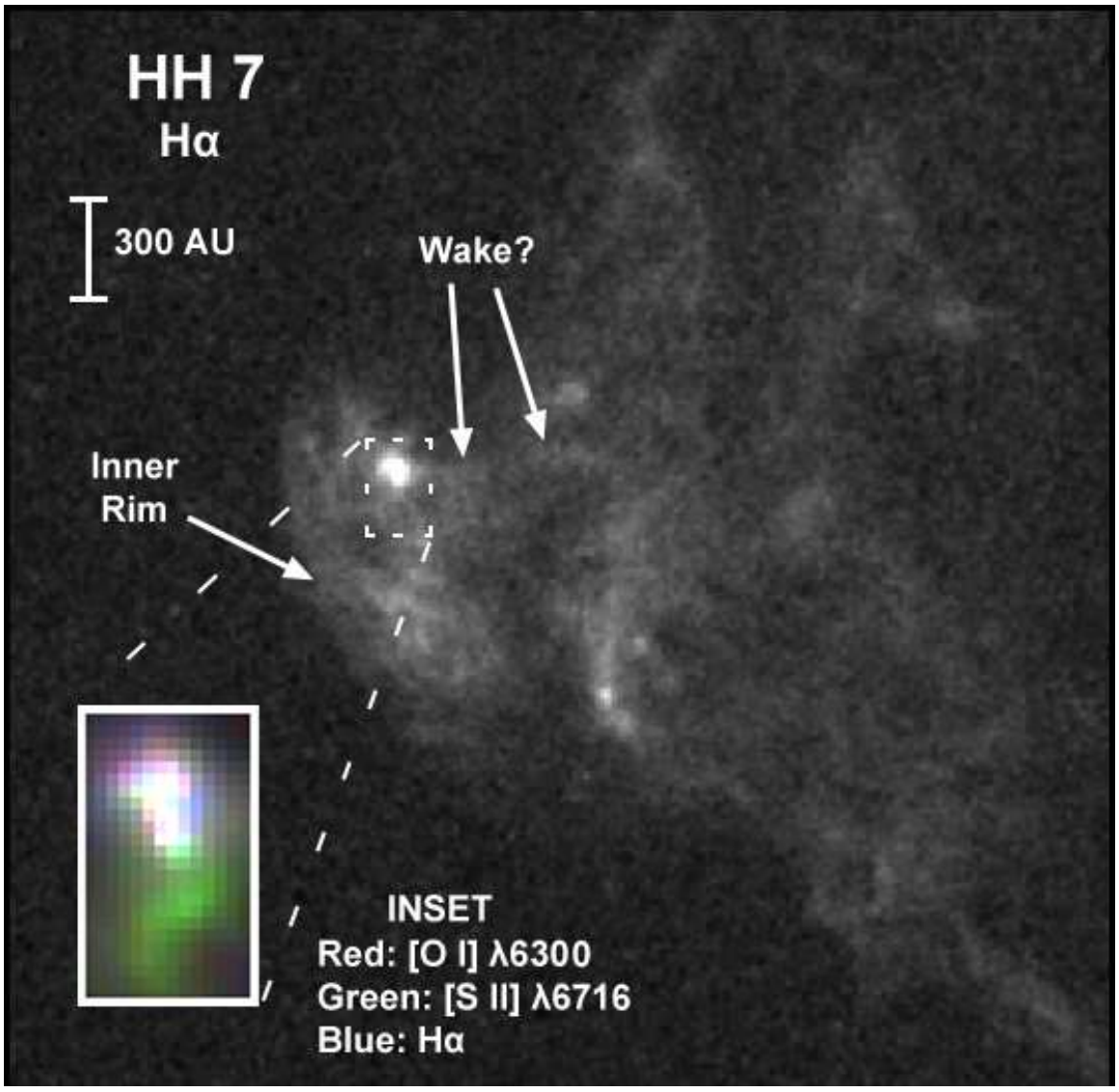


Fig. 6.— Epoch 2 images of HH 7 (greyscale; Hα) and of the bright knot embedded within its leading bow shock (color inset; composite). The bright knot shows structure down to the resolution limit of HST. The bright knot and its possible wake suggest the jet has broken into small clumps by the time it enters the leading HH 7 bow shock. The inner rim marks the extent of the optical line emission (see also Fig 2).

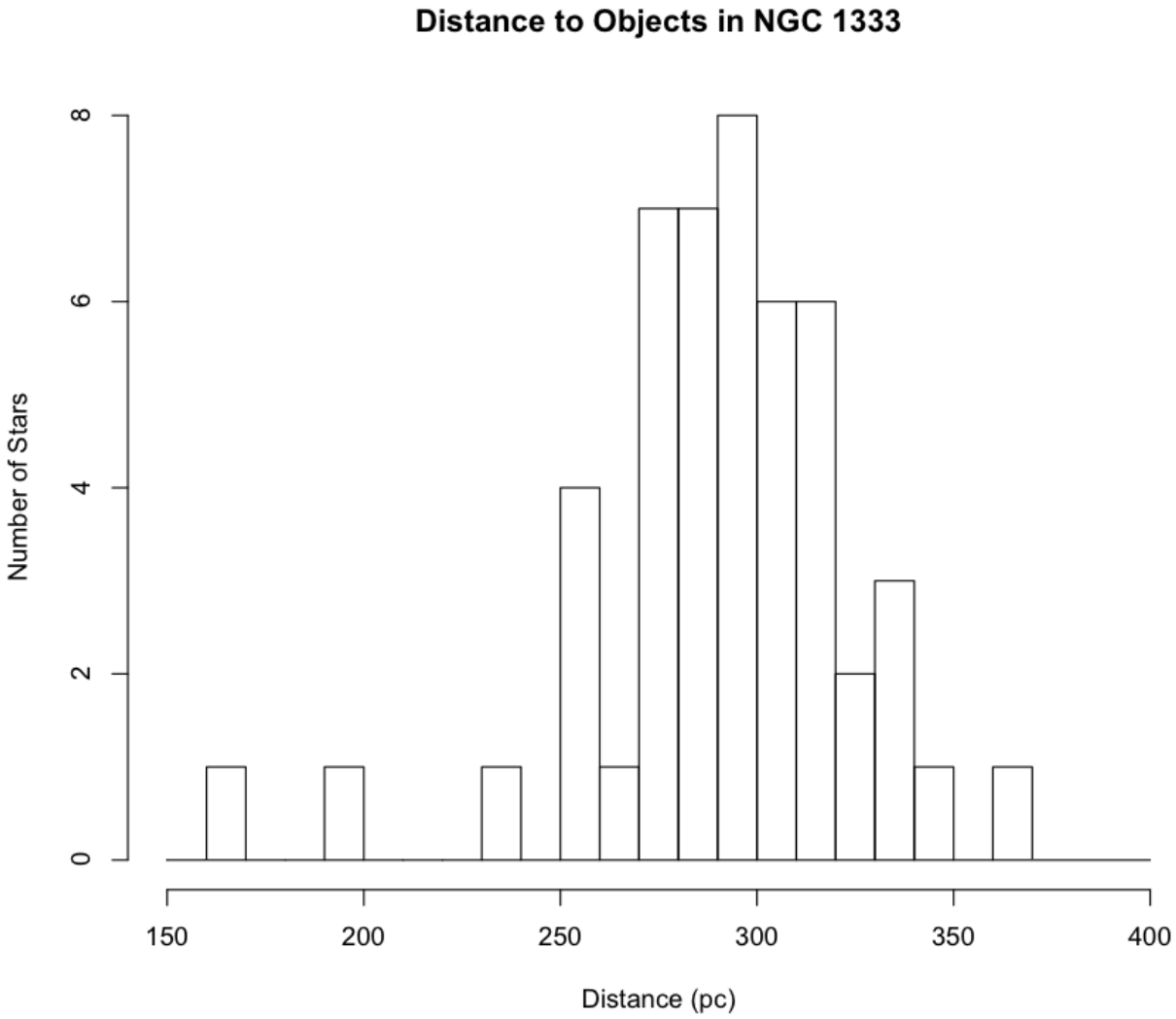


Fig. 7.— GAIA-DR2 distances for the sources in (Foster et al. 2015).

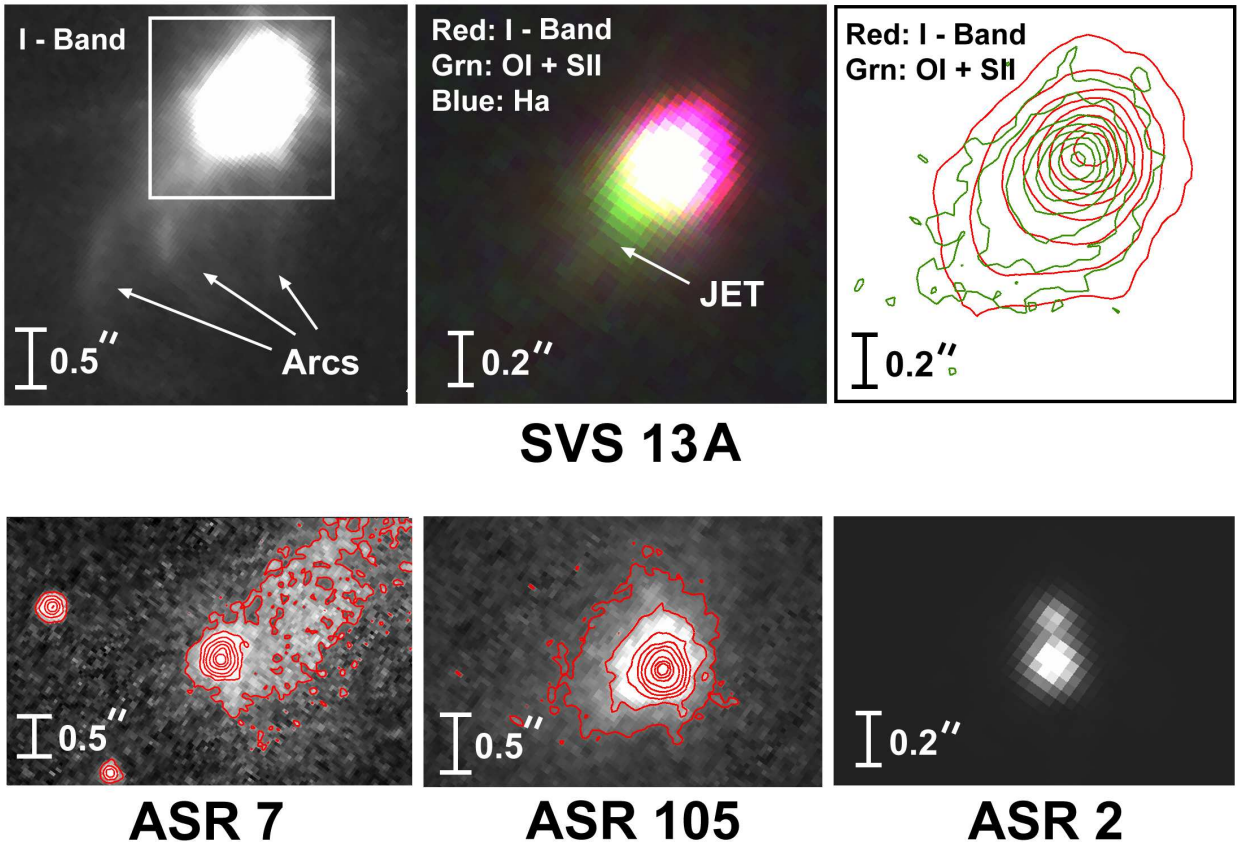


Fig. 8.— Compilation of stellar objects in the field of view that are not simple point sources. North is up and east to the left in all images and adjacent contours are a factor of two. The scale bars of 0.2″ and 0.5″ correspond to 60 AU and 300 AU, respectively. Top: SVS 13A, the driving source of the HH 7-11 flow, has several curved arcs in the I-band image and a microjet visible as an extension to the southeast of the source in the [O I] + [S II] composite. Bottom: Both ASR 105 and ASR 7 show extended cavities in their I-band images, while ASR 2 is a close binary in all the narrowband and broadband images (F656N shown here).

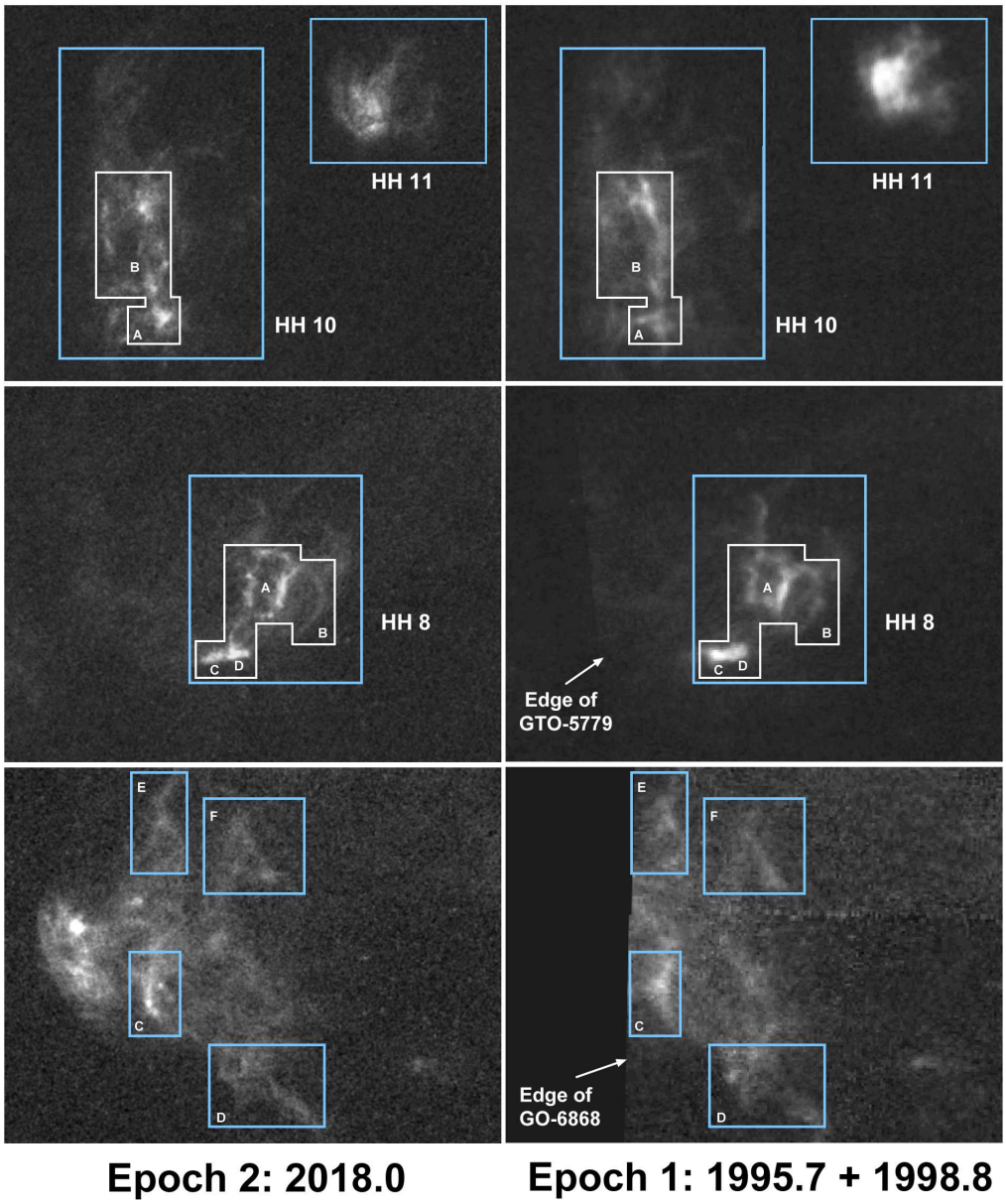


Fig. 9.— Proper Motions and Variability in HH 7-11. The images are Hα, and combine GTO-5779 and GO-6868 to produce epoch 1. Our new images are shown at left as epoch 2. White boxes in the images are shown for reference purposes only, and are fixed in the sky. These boxes highlight secular variability if the reader glances quickly between the left and right panels. The light-blue boxes, also fixed regions of the sky, are used for the proper motion measurements in Table 1.

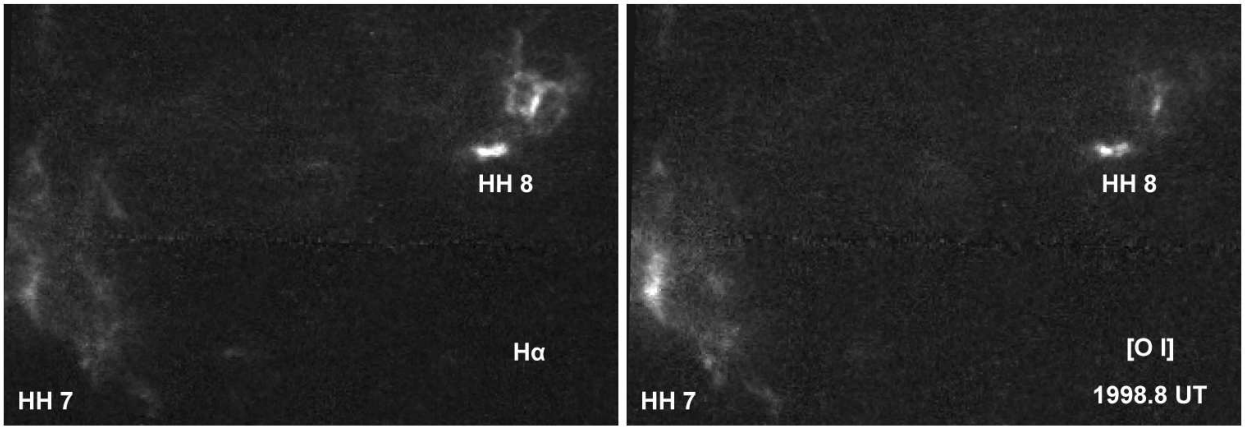


Fig. 10.— Proper Motions and Variability in HH 7 and HH 8. An animated version of this figure is available. In the animation, the images for Hα (left) and [O I] (right) switch between epoch 1 and epoch2.

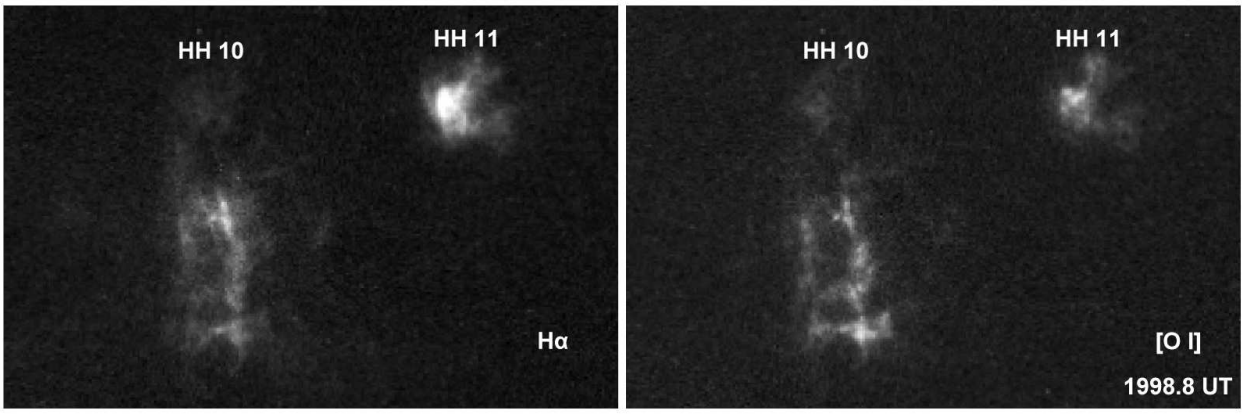


Fig. 11.— Same as Fig. 10 but for HH 10 and HH 11. In the animated version, Hα (left) and [O I] (right) alternate between epoch 1 and epoch2.

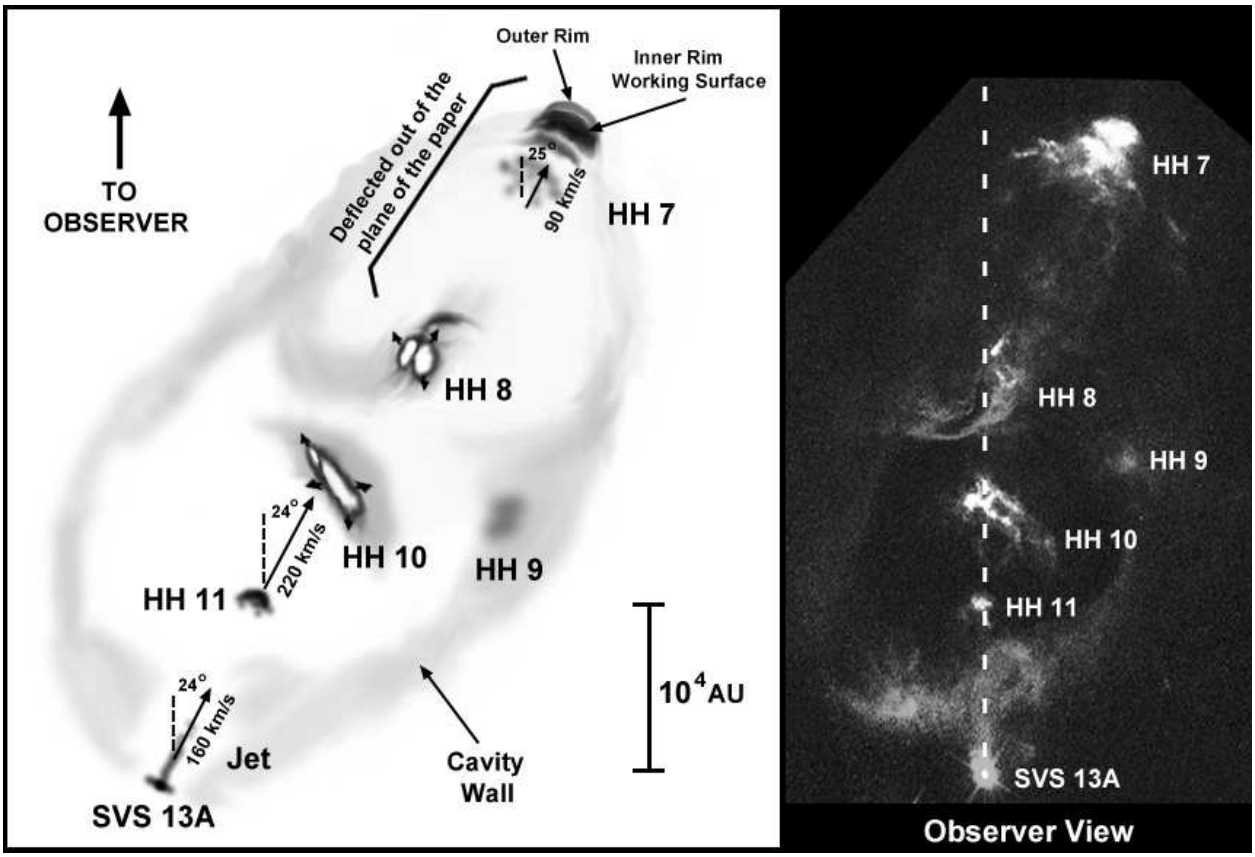


Fig. 12.— Schematic of the HH 7-11 Outflow. Left: HH 11 moves in the plane of the diagram at an angle of $\sim$ 24 degrees to the line of sight. HH 8 and HH 10 are variable structures that trace where the jet interacts with obstacles along its path, and HH 7 is the terminal bow shock. Jet gas incident to HH 7 also moves at $\sim$ 25 degrees to the line of sight, but is tilted out of the plane of the paper, accounting for a shift of 55 degrees in the direction of proper motion relative to that of HH 11. Right: Greyscale image of Fig. 1, showing the outflow from the observer's reference frame.

Table 1. Proper Motions in the HH 7-11 Jet

Object[a]	$\mu_{\rm RA}$[b]	$\mu_{\rm DEC}$[c]	μ (km s^{-1})[d]
HH 7C	2.7 ± 0.4	0.1 ± 0.4	38 ± 7
HH 7D	0.9 ± 0.4	0.4 ± 0.4	14 ± 7
HH 7E	0.5 ± 0.4	-0.7 ± 0.4	12 ± 7
HH 7F	1.2 ± 0.4	0.6 ± 0.4	19 ± 7
HH 8	0.2 ± 0.3	0.1 ± 0.3	< 6
HH 10	0.2 ± 0.3	-0.2 ± 0.3	< 6
HH 11	3.9 ± 0.3	-5.0 ± 0.3	91 ± 6

[a:]Objects defined by blue boxes in Fig.9

[b:]Proper motion in RA (arcsec/century)

[c:]Proper motion in DEC (arcsec/century)

[d:]Tangential velocities, assuming a distance of 300 pc